Mon. Not. R. Astron. Soc. **000**, 1–16 (2014) Printed 17 December 2014 (MN LATEX style file v2.2)

3-D Kinematics of the near-IR HH 223 outflow in L723

R. López,[1⋆] J. A. Acosta-Pulido,[2,3⋆] R. Estalella,[1⋆] G. Gómez[4,2⋆], and B. García-Lorenzo[2,3⋆]

[1]*Departament d'Astronomia i Meteorologia (IEEC-UB), Institut de Ciències del Cosmos, U. de Barcelona, Martí i Franquès 1, E-08028 Barcelona, Spain*
[2]*Instituto de Astrofísica de Canarias, E-38200 La Laguna, Spain*
[3]*Departamento de Astrofísica, Universidad de La Laguna, E-38205, Tenerife, Spain*
[4]*GTC Project Office, GRANTECAN S.A. (CALP), E-38712 Breña Baja, La Palma, Spain.*

arXiv:1412.4939v1 [astro-ph.SR] 16 Dec 2014

Accepted 2014 December 4. Received 2014 December 1; in original form 2014 November 12

ABSTRACT

In this work we derive the full 3-D kinematics of the near-infrared outflow HH 223, located in the dark cloud Lynds 723 (L723), where a well-defined quadrupolar CO outflow is found. HH 223 appears projected onto the two lobes of the east-west CO outflow. The radio continuum source VLA 2, towards the centre of the CO outflow, harbours a multiple system of low-mass young stellar objects. One of the components has been proposed to be the exciting source of the east-west CO outflow.

From the analisys of the kinematics, we get further evidence on the relationship between the near-infrared and CO outflows and on the location of their exciting source. The proper motions were derived using multi-epoch, narrow-band H_2 (2.122 μm line) images. Radial velocities were derived from the 2.122 μm line of the spectra. Because of the extended ($\sim$ 5 arcmin), S-shaped morphology of the target, the spectra were obtained with the Multi-Object-Spectroscopy (MOS) observing mode using the instrument LIRIS at the 4.2 m William Herschel Telescope. To our knowledge, this work is the first time that MOS observing mode has been successfully used in the near infrared range for an extended target.

Key words: ISM: jets and outflows – ISM: individual: LDN 723 – ISM: individual: HH 223

1 INTRODUCTION

The isolated dark cloud Lynds 723 (L723), located at a distance of 300 $\pm$150 pc (Goldsmith et al. 1984) is one of the few sites where a well-defined quadrupolar CO outflow has been reported (two separate pairs of red-blue lobes; Lee et al. 2002 and references therein). The 3.6 cm radio continuum source VLA 2 (Anglada, Rodríguez, & Torrelles 1996), located towards the centre of the CO outflow, harbours the low-mass source that powers the outflow. Carrasco-González et al. (2008) and Girart, Rao & Estalella (2009) report that VLA 2 is a multiple system of four (VLA 2A, 2B, 2C and 2D) young stellar objects (YSOs), and that one of the components (VLA 2A) is powering the east-west CO outflow. Later on, Girart, Rao & Estalella (2009) detect dust emission at 1.35 mm, resolved into two components (SMA 1 and SMA 2). SMA 2, in a more evolved stage, is harbouring the multiple low-mass protostellar system VLA 2. In addition, they report emission from the SiO 5–4 line towards the SMA sources, which shows an elongated morphology that follows the direction of the east-west CO outflow near the exciting source as well as that of the near-infrared and optical outflows reported in L723.

The protostellar system embedded in SMA 2 seems to be associated with the large-scale outflows detected in other wavelength ranges, as proposed from previous deep narrow-band images of the L723 field. In the optical range, it drives the Herbig-Haro (HH) object 223 of the Reipurth Catalogue[1] first detected by Vrba et al. (1986) as a "linear emission feature", and later resolved into several knots by López et al. (2006). The spectra of these knots are characteristic of shock-excited gas, as revealed from long-slit spectroscopy (López et al. 2009). The emission of the knots show a complex pattern, both in its kinematics and physical conditions, as derived from Integral Field Spectroscopy (IFS) observations by López et al. (2012). In the near-infrared range, Palacios & Eiroa (1999) detect in a *K*-band image several H_2 emission nebulae, located at both sides of VLA 2 . Later on, López et al. (2010) obtain deep images of the L723 field through narrow-band filters centred on the [Fe II] 1.644 μm and H_2 2.122 μm lines. The images show a set of H_2 emission features, distributed from the southeast to the

⋆ E-mail: rosario,robert@am.ub.es; jap,bgacia@iac.es; gabriel.gomez@gtc.iac.es

[1] Reipurth, B.: 1999, A general catalogue of Herbig-Haro objects, 2. edition, http://casa.colorado.edu/hhcat

© 2014 RAS

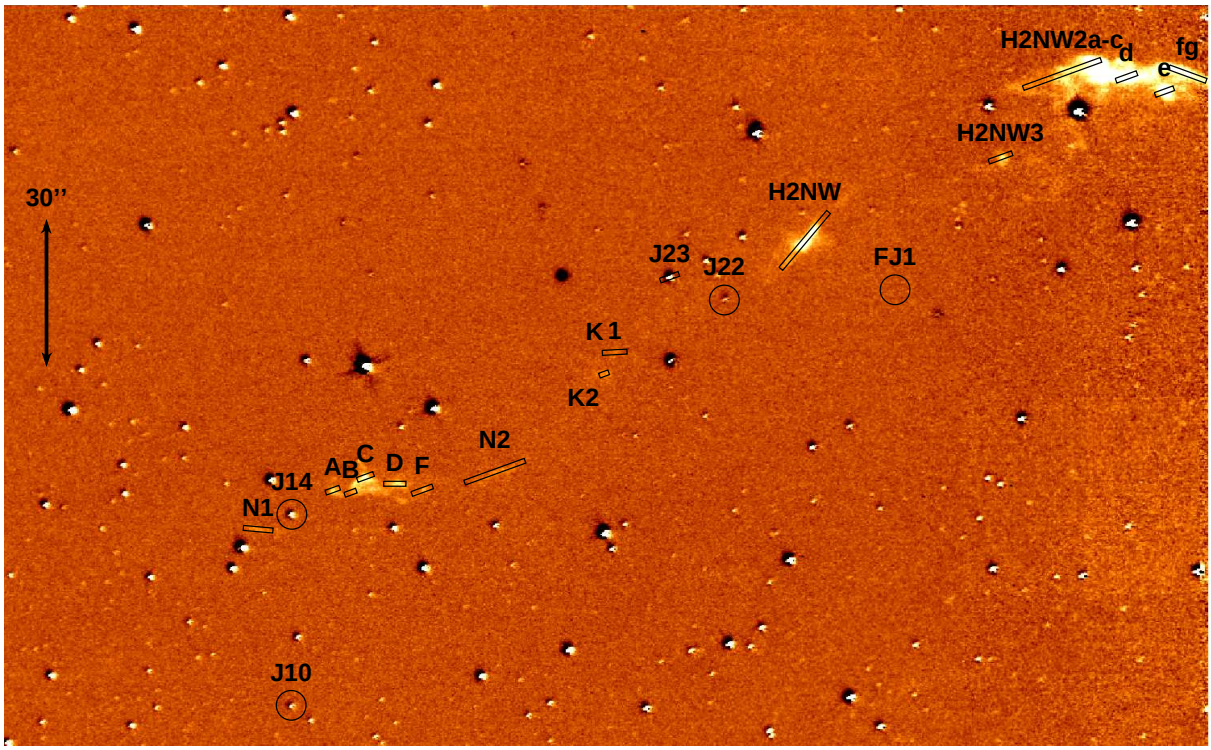

Figure 1. Image of the L723 field obtained wiht LIRIS through the H_2 2.122 μm line filter (the continuum has been substracted). The rectangles represent the position of the slitlets of the mask designed for the Multi-Object Spectroscopy (MOS) observations. The knots of HH 223 enclosed in the corresponding slitlet of the mask have been labeled according to the nomenclature of López et al. (2010). An additional slitlet, labeled J23 was included to check the individual frame quality. The four circular appertures, labeled J10, J14, J22 and FJ1, used for mask centering, are also drawn. North is up and east is to the left.

northwest of the L723 field, extending along $\sim$ 5 arcmin ($\sim$ 0.5 pc for a distance of 300 pc). The H_2 emission features are found projected onto the lobes of the east-west CO outflow, with a S-shaped morphology, and are proposed to form part of a H_2 outflow, which also has optical counterpart at the regions with low visual extinction, given rise to the HH object 223. In contrast, the [Fe II] 1.644 μm image only shows emission associated with the HH object 223, which could be tracing the densest, high-ionized and lower extinction region of the outflow.

The 3-D kinematics (i. e. including proper motions and radial velocities) is a more robust tool than the outflow morphology for a reliable identification of the driving source of the outflow: the direction of the motions of the outflow features points to the position of the driving source. However, the kinematics of the near-infrared HH 223 outflow remained unknown up to date. With the aim of obtaining further evidence on the relationship between the H_2 and the CO outflows of L723, as well as to check the location of the source driving the optical/near-infrared/millimetre outflows, we conducted an in-depth study of the kinematics of the near-infrared outflow. We derived proper motions and radial velocities of the near-infrared emission features, extending at both sides of the radio-continuum sources. The proper motions were found from multi-epoch imaging of the L723 field, obtained with the same instrumental configuration. The radial velocity field was derived from *K*-band spectroscopy, using the bright H_2 2.122 μm line. Because of the extended S-shape morphology of the H_2 emission, the Multi-Object-Spectroscopy (MOS) observing mode results more efficient than long-slit mapping if we want to cover most emission features along the outflow in a reasonable amount of observing time. The instrument LIRIS at the WHT offers this observing mode in the near-infrared range. LIRIS-MOS observing mode has been widely used to get spectra of point-sources in crowded fields, although this is the first time that it has been used to collect spectra of extended targets like the nebular emission features in the field of L723. The use on extended targets introduces some complexities, such as the slit mask design and the data reduction and calibration procedures to be followed.

2 OBSERVATIONS, DATA REDUCTION AND CALIBRATION

Imaging and Multi-Object Spectroscopy observations were made with the instrument LIRIS (Long-Slit Intermediate Resolution Infrared Spectrograph; Acosta Pulido et al. 2003; Manchado et al. 2004) at the 4.2 m Williams Herschel Telescope (WHT) of the Observatorio del Roque de los Muchachos (ORM, La Palma, Spain). LIRIS is equipped with a Rockwell Hawaii 1024 $\times$ 1024 HgCdTe array detector. The spatial scale is 0.25 arcsec pixel^{-1}, giving an image field of view (FOV) of 4.27 $\times$ 4.27 arcmin^2. Imaging and spectroscopic data were processed using the package *lirisdr*[2] developed by the LIRIS team within the IRAF[3] environment.

[2] http://www.iac.es/project/LIRIS

[3] IRAF is distributed by the National Optical Astronomy Observatories, which are operated by the Association of Universities for Research in Astronomy, Inc., under cooperative agreement with the National Science Foundation.

Table 1. Observation Log

Imaging

Date	Grism	Exp. Time (s)	Seeing (arcsec)
2006-07-20	H_2	1800	0.8
2010-06-22	H_2	1800	1
2012-07-26[a]	H_2	3100	1

[a] Obtained under Director's Discretionary Time of Spain's Instituto de Astrofísica de Canarias

MOS Spectroscopy

Date	Grism	Exp. Time[b] (s)	Seeing (arcsec)
2009-08-29	HR_K	6×600	0.7
2010-06-22	HR_J	6×600	1
2010-06-22	HR_H	6×600	1

[b] On-source integration time

Table 2. Configuration of the mask

Knot HH 223-	Slitlet ID	Length (arcsec)	Center Position α_{2000}	δ_{2000}	PA (deg)
N1	s1	6.0	19 17 59.034	+19 11 42.10	−95
A	s2	3.0	19 17 57.970	+19 11 50.02	−70
B	s3	2.5	19 17 57.717	+19 11 49.51	−70
C	s4	3.5	19 17 57.501	+19 11 52.71	−70
D-E	s5	4.5	19 17 57.087	+19 11 51.33	−90
F	s6	4.5	19 17 56.697	+19 11 50.04	−70
N2	s7	13.0	19 17 55.660	+19 11 53.80	−70
K2	s8	2.0	19 17 54.100	+19 12 13.60	−70
K1	s9	5.0	19 17 53.950	+19 12 18.00	−87
star J23	s10	4.0	19 17 53.170	+19 12 33.20	−75
H2-NWab	s11	15.0	19 17 51.235	+19 12 40.67	−40
H2-NW3	s12	5.0	19 17 48.440	+19 12 57.50	−70
H2-NW2abc	s13	16.7	19 17 47.560	+19 13 14.40	−70
H2-NW2d	s14	4.5	19 17 46.643	+19 13 13.81	−70
H2-NW2e	s15	4.0	19 17 46.101	+19 13 10.85	−70
H2-NW2fg	s16	8.0	19 17 45.771	+19 13 14.40	−110

2.1 Imaging

Deep narrow-band images of the L723 field through a filter centred on the H_2 2.122 μm line were obtained at three different epochs (2006 July 20, 2010 June 22 and 2012 July 26). The observing strategy consisted of a 5-point dithering pattern. Due to the elongated morphology of the target, we used a E-W offset three times larger than the one used along the N-S direction. The reduction process included sky subtraction, flat-fielding, correction of geometrical distortion, and finally combination of frames using the common "shift-and-add" technique. This final step consisted in dedithering and co-addition of frames taken at different dither points to obtain a mosaic covering a field of $\sim$ 5 × 5 arcmin^2, which includes the HH 223 H_2 outflow. Astrometric calibration in each final image was made using the coordinates from the 2MASS All Sky Catalogue of ten field stars well distributed on the observed field. The rms of the transformation was 0.04 arcsec in both coordinates.

2.2 Multi Object Spectroscopy

We obtained spectra of the line-emitting nebulosities forming the HH 223 H_2 outflow, which extends over 5.5 arcmin (equivalent to $\sim$ 0.5 pc for a distance of 300 pc) PA following a S pattern with a postion angle (PA) $\simeq$ 110°. The identification of the H_2 filaments and clumps can be found in López et al. (2010). In order to be more efficient for collecting the spectra, we used the MOS mode of LIRIS. The observations were performed at two different epochs (see Table 1 for details), using the same MOS mask at the same nominal positioning. The FOV of LIRIS together with the particularly elongated morphology of the outflow permit to cover most of the line emitting regions with the slitlets relatively well aligned (see Fig. 1). This fact guarantees a rather consistent wavelength coverage for most of them. The designed mask had 16 slitlets: 15 of them were located to cover the outflow features, and one more (number 10) was positioned onto a star, which was used as a reference target. The aim of using a reference target was twofold: to register the offset between different frames, and to assess individual frame quality. In addition, the mask design included holes, placed at the position of three relatively bright field stars, to support the pointing and acquisition process of the field. Each slitlet was 1 arcsec wide, and its length ranged from $\sim$ 1.5 to 16 arcsec, depending on the morphology of the corresponding feature to be sampled (see Fig. 1 and Table 2). The orientation of each slitlet was slightly different, which introduces relative tilting of the spectral lines among the spectra of different slitlets. Note that this mask was the first one designed with the unusual requirement to have slitlets with different relative orientations.

Spectra were obtained using the designed mask and the 3 medium-resolution (R $\simeq$ 2500) grisms, covering the nominal spectral ranges from 1.18 to 1.35 μm, from 1.53 to 1.79 μm, and from 2.07 to 2.44 μm, in the *J*, *H* and *K* spectral windows, respectively. Total on-source integration time was 1 hr, split in individual exposures of 600 s to avoid saturation by the bright sky lines and to compensate for their time variability. The observations were perfomed repeating the sequence Object-Sky (OSOS). The sky exposures were obtained in an empty field, offset by $\sim$ 1 arcmin, roughly perpendicularly to the outflow axis, since the observed field is crowded and our targets are extended and close to each other.

The data reduction process of this dataset was rather complex and combined *lirisdr*/IRAF standard procedures with more dedicated correction steps developed in IDL. For the standard procedures we used the routines available for the LIRIS MOS mode in the *lirisdr* package. The first step was to determine and correct the geometrical distortions along the spatial axis in order to have the spectra aligned within the CCD rows. Dome white lamp (dome flats, hereafter) spectra were used to determine the correction. Next, we used the a-priori mask design information to trace the slitlet positions and their limits from a distortion-free dome–flat frame. Then the 2-D spectra from each slitlet were extracted following the limits determined previously and were calibrated independentely. The wavelength calibration was determined from argon and xenon lamp exposures obtained with the same instrument configuration through the MOS mask. The arc spectra for each slitlet were extracted in the way described before. The initial wavelength calibration was determined as in the "long-slit case" following the usual tasks in IRAF (i.e. combining *identify, reidentify* and *fitcoords*). The accuracy of the wavelength calibration was then checked using a set of bright, isolated OH sky lines present in the observed wavelength ranges. It was noted that wavelength offsets were present, which is expected due to spectrograph flexures. The determination of radial veloci-

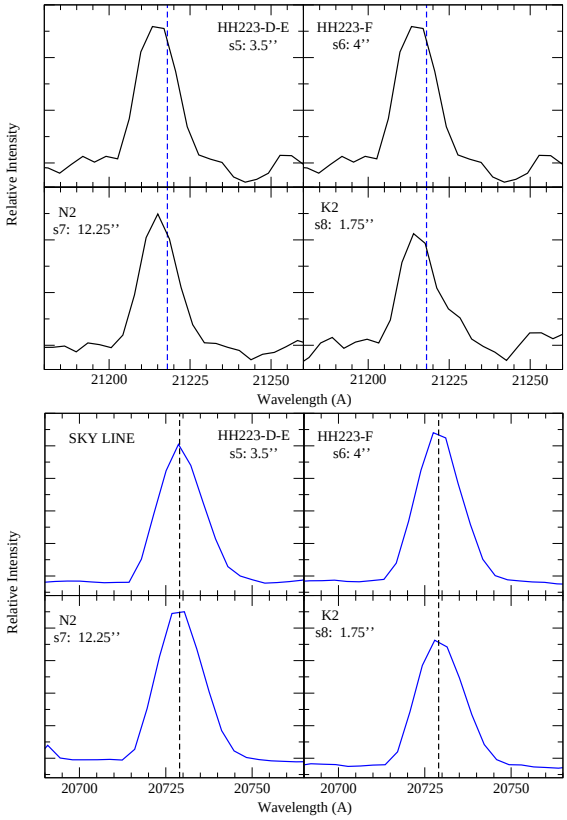

Figure 2. Profiles of the H_2 line emission at H_2 2.122 μm (top) and of the OH sky line at 2.073 μm (bottom) for the spectra averaged within the slitlets labeled in the panel. Dashed lines indicate the position that corresponds to the rest wavelength.

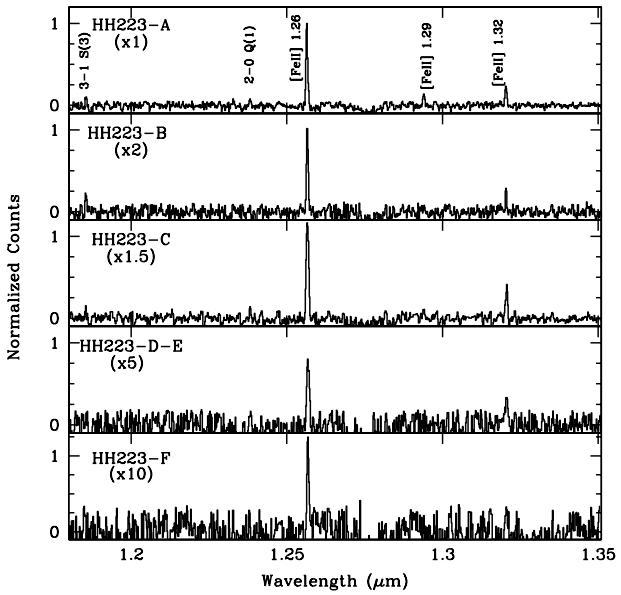

Figure 3. *J*-band spectra of the slitlets covering the knots with detected emission lines of the HH 223 H_2 outflow, obtained by averaging the signal within the corresponding slitlet. Intensities have been scaled relative to the [Fe II] 1.257 μm line intensity peak of the HH223-A knot.

ties from emission lines is a crucial aspect of the present work, therefore we needed to refine the wavelength calibration by applying an offset determined from the wavelength difference observed in the mentioned OH sky lines. After this correction was applied, the accuracy reached for the wavelength calibration was better than 0.35 Å in all the observed wavelength range (i. e. 4.9 km s^{-1} for the H_2 2.122 μm, and 6.3 km s^{-1} and 8.3 km s^{-1} for the 1.644 μm and 1.257 μm [Fe II] emission lines).

A check of the reliability of the wavelength calibration in the wavelength range close to the line used to derive the kinematics (H_2 2.122 μm) can bee seen in Fig. 2, which shows the line profiles of this line (top panels) and of the OH 2.073 μm sky line (bottom panels) of the spectra obtained by averaging the signal within the full aperture of the slitlet labeled in each of the panels. The position of the corresponding rest wavelength has been marked with the dashed vertical line. Note that the emission appears shifted from the rest wavelength position in the case of the H_2 2.122 μm line, while it appears centred at the rest wavelength for the sky line, as should be expected. We then concluded that the wavelength calibration was accurate enough to derive reliable kinematics of the outflow emission using the H_2 2.122 μm line.

Next we performed the sky subtraction to the science frames using an average sky spectrum obtained from the adjacent sky frames. The resulting sky-subtracted spectrum showed large residuals coincident with bright OH sky lines. In order to improve the results we followed an approach similar to that developed by Davies (2007): first we separated the OH emission lines from the sky continuum. The sky continuum was modelled by a smooth function (a polynomial function of degree 4 is usually a good solution). In order to scale properly the OH emission spectrum we divided the spectral range into segments which correspond to different vibrational transitions of the OH molecule. We found the scaling factor for each of the segments that minimized the difference between the sky and the object spectra. Finally, the sky spectrum was subtracted from the 2-D object extracted spectra, and we combined them into an average spectrum for each slitlet. Any possible offsets along the slit direction were derived from the relative positions of the reference stars and then taken into account before the object frames were combined.

3 RESULTS AND DISCUSSION

We obtained the one-dimensional spectrum for each of the 15 slitlets covering the nebulosities of the HH 223 H_2 outflow by averaging the signal within the corresponding slitlet (i. e. within a rectangular aperture of 1 arcsec width and a slit length ranging from $\sim$ 2 arcsec to $\sim$ 16 arcsec, see Table 2). The spectra in the *J*, *H* and *K* bands are shown in Figs. 3, 4 and 5, respectively. In order to search for variations at scales smaller than the length of the slitlets, we extracted, in addition, the one-dimensional spectra of each of the H_2 features identified along the HH 223 outflow. The kinematics of HH 223 was derived from the spectra. The spatial brightness distribution of neutral and ionized gas outflow was also explored from the 2-D MOS spectra (see Fig 6).

3.1 Emission brightness distribution

3.1.1 The neutral outflow

In the near-infrared, the emission of the neutral gas of the HH 223 outflow is traced by the H_2 lines. In the observed wavelength range,

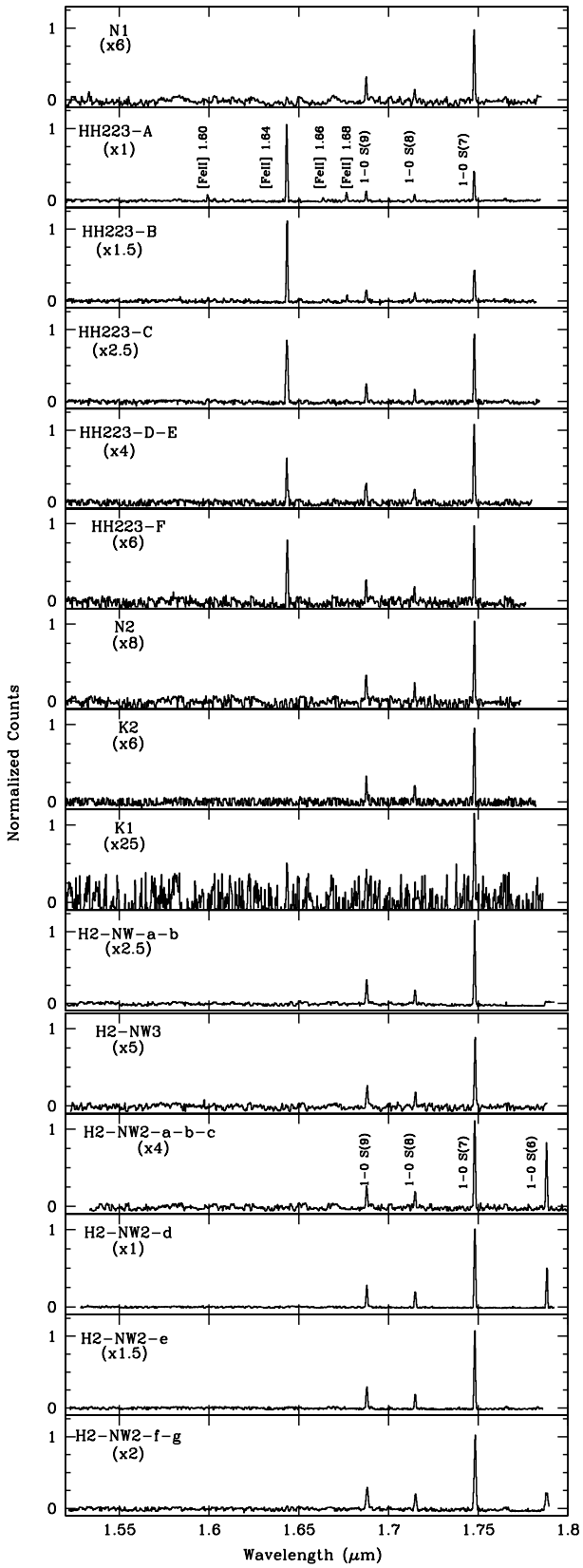

Figure 4. Same as Fig. 3, but for the *H*-band spectra. Intensities have been scaled relative to the H_2 1.75 μm line intensity peak of the H2-NW2-d knot.

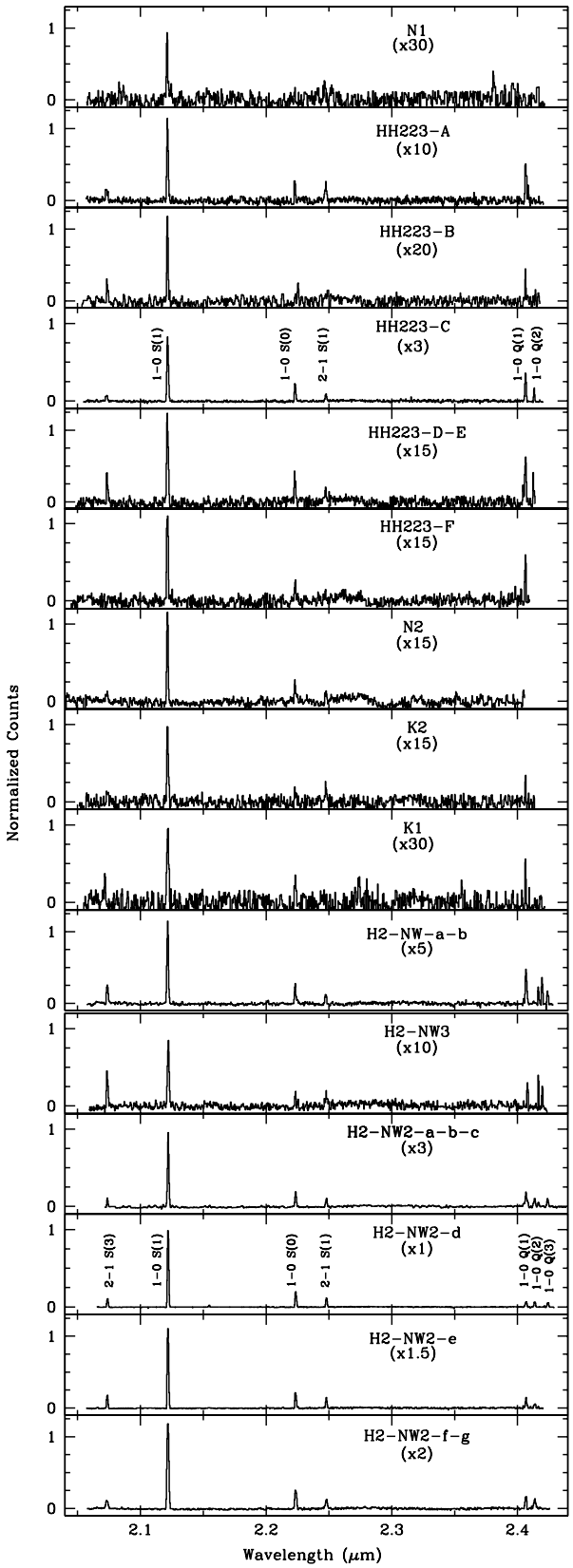

Figure 5. Same as Fig. 3, but for the *K*-band spectra. Intensities have been scaled relative to the 2.122 μm line intensity peak of the H2-NW2-d knot.

all the H_2 transitions we detected correspond to those with the lowest excitation levels ($E \leqslant 15000$ K).

As can be seen from Figs. 4 and 5 the bright H_2 $\upsilon = 1$–0 $S(7)$ 1.748 μm and H_2 $\upsilon = 1$–0 $S(1)$ 2.122 μm emission lines were detected with high signal-to-noise (SNR $\geqslant 10$) in all the spectra. Other H_2 transitions were also detected in several slitlets, and have been marked in the figures. In the *K* band, the Q-branch emission lines at 2.4 μm, lying at the edge of the covered spectral range, were found in most of the slitlets. Additional H_2 lines, e. g. the $\upsilon = 1$–0 $S(0)$ 2.224 μm and the $\upsilon = 2$–1 $S(1)$ 2.248 μm were found in several slitlets (these onto the knots HH 223-A to -F and -H2-NW, -H2-NW2), but were detected with a lower SNR (by a factor ~ 5 and ~ 10, respectively) relative to the SNR of the 2.122 μm). In the *H* band, several H_2 transitions were detected in most of the slitlets (from the $\upsilon = 1$–0 $S(6)$ 1.788 μm to the $\upsilon = 1$–0 $S(9)$ 1.687 μm lines). However, only the bright 1.748 μm line was detected at the slitlet S9, positioned on HH 223-K1, the knot closest to the site where the outflow exciting source is embedded. Finally, in the *J* band, only the H_2 $\upsilon = 3$–1 $S(3)$ 1.185 μm and $\upsilon = 2$–0 $Q(1)$ 1.238 μm lines were detected (SNR $\simeq 5$) in HH 223-A. The lack of detection of the *J* band H_2 lines in most of the knots can be due mainly to extinction, because these knots are more embedded in the cloud. Note that most of the bright knots identified in the *K* band (e. g. HH 223-NW and -NW2) lack of an optical counterpart. This can be also the case of HH 223-K1. At this position, the high extinction could prevent the detection of the other H_2 lines lying at the *H* band, except the bright 1.748 μm line.

3.1.2 The ionized outflow

The emission of the ionized gas of HH 223 is traced by the [Fe II] lines.The [Fe II] lines were detected only through the slitlets positioned on the HH object 223 (i.e., knots HH 223-A to -F, the knots having an optical counterpart). The bright [Fe II] 1.257 μm and 1.644 μm lines were detected in all these knots. Other weaker [Fe II] transitions (e. g. at 1.600, 1.664 and 1.677 μm, in the *H* band, and at 1.295 and 1.321 μm in the *J* band) were only detected in the spectrum of the knot HH 223-A. The fact that the [Fe II] transtions were only detected in a few knots of the near-infrared HH 223 outflow is consistent with what was found from previous deep narrow-band *H*-band images of the field (López et al. 2010).

The spatial brightness distribution of the [Fe II] and H_2 emissions are not fully coincident, as can be seen from Fig. 6 (left panels) by comparing the PV maps of the [Fe II] 1.644 μm (red contours) and H_2 2.122 μm (black contours) line emissions. The greater discrepancies are found for the emissions acquired through the slitlets S3 and S4, positioned on the knots HH 223-B and HH 223-C. In spite of the [Fe II] (*H* band) and H_2 2.122 μm (*K* band) spectra being obtained at two different observing runs, we want to remark that the observed displacements between these emissions could not be caused by a difference in the positioning of the mask on the field in each of the observing runs. To support this assertion, Fig. 6 also displays the PV map obtained from the *H*-band H_2 1.748 μm line emission (left panels, green contours). In general, the spatial distribution of the emission from the 2.122 μm line appears more extended than the emission from the 1.748 μm line, although its spatial brightness distribution is closely coincident with that of the 2.122 μm line. Hence, the spatial displacement found between the spatial brightness distribution of the ionized ([Fe II]) and neutral (H_2) emissions is believed to be reliable.

The knots HH 223-A to -F are far away from the location of the powering source of the outflow (close to HH 223-K1). Hence, the origin of the [Fe II] emission in these knots cannot be the gas heated by a close protostar. The most plausible heating mechanism is the presence of shocks with appropriate strength to ionize and excite the gas outflow. On the other hand, it is very unlikely that both the [Fe II] and H_2 emissions originate from the same parcel of shocked gas, because each of these emissions trace shocks with completely different degree of excitation, which are seen either in projection or are unresolved within the same beam. It should be noted that the optical counterpart of the HH 223-A to HH 223-F knots have revealed to show a rather complex kinematic pattern, as derived from an IFS mapping with more complete coverage (López et al. 2012). The IFS results suggest the presence of a set of shocks of complex morphology, unresolved with the observed beam resolution. In this scenario, the [Fe II] emission may be tracing the sites where the interaction, either between different episodes of mass ejection (like internal working surfaces) or between the supersonic gas and dense clumps of the wall cavity, is strong enough to excite the [Fe II] transitions.

We expected to detect [Fe II] emission in the spectra obtained along the HH 223-K1 feature, since the gas would be ionized given the proximity to the outflow exciting source. However, we failed to detect [Fe II] emission in any of the observed bands. The non-detection of [Fe II] emission at this position, and for the rest of the HH 223 knots, could be caused by a higher extinction than in HH 223A-F. The non-detection of optical counterparts for all of these knots favours this hypothesis.

3.2 Radial velocities

The main aim of this work is to establish the kinematics of the near-infrared HH 223 outflow by deriving both radial velocity and proper motions along all its knots, covering ~ 5 arcmin in the E-W direction. Because the emission of the ionized gas (traced by the [Fe II] lines) was only detected in part of the outflow (along ~ 30 arcsec), we focused our study on the full kinematics of the neutral gas, traced by the H_2 emission in the *K* band, where the effects of the extinction are lower than in the other two bands, and the most deeply embedded knots are detected in the images. In addition, we also derived the radial velocity of the ionized gas from the brightest [Fe II] lines in the *J* and *H* bands at the knots HH 223-A to HH 223-F.

In order to derive the radial velocity field, we obtained the line centroid from a Gaussian fit to the H_2 2.122 μm line. Note that this line is well separated from any bright OH sky line. Hence, any residual sky line resulting from an imperfect sky subtraction does not affect the velocity measurements. Furthermore, this line is the brightest one in the observed *K* spectral range, and it is also the only line detected in all the knot spectra with a high SNR (ranging from 10 to 150). As mentioned before, there are other H_2 emission lines lying in the observed spectral range, but they do not seem so suitable to trace the outflow kinematics. The weaker 2.224 μm and 2.248 μm lines were not detected through all the slitlets, or have lower SNR (by a factor ~ 5 and ~ 10, respectively) than that of the 2.122 μm line. The Q-branch lines are brighter, but they lie at the edge of the spectral range covered with the spectral configuration used (at 2.4 μm), and the accuracy reached in the wavelength calibration was lower (rms of 0.40 Å, ~ 5.7 km s^{-1}) than that achieved for the 2.122 μm line emission (rms of 0.25 Å, ~ 4 km s^{-1}).

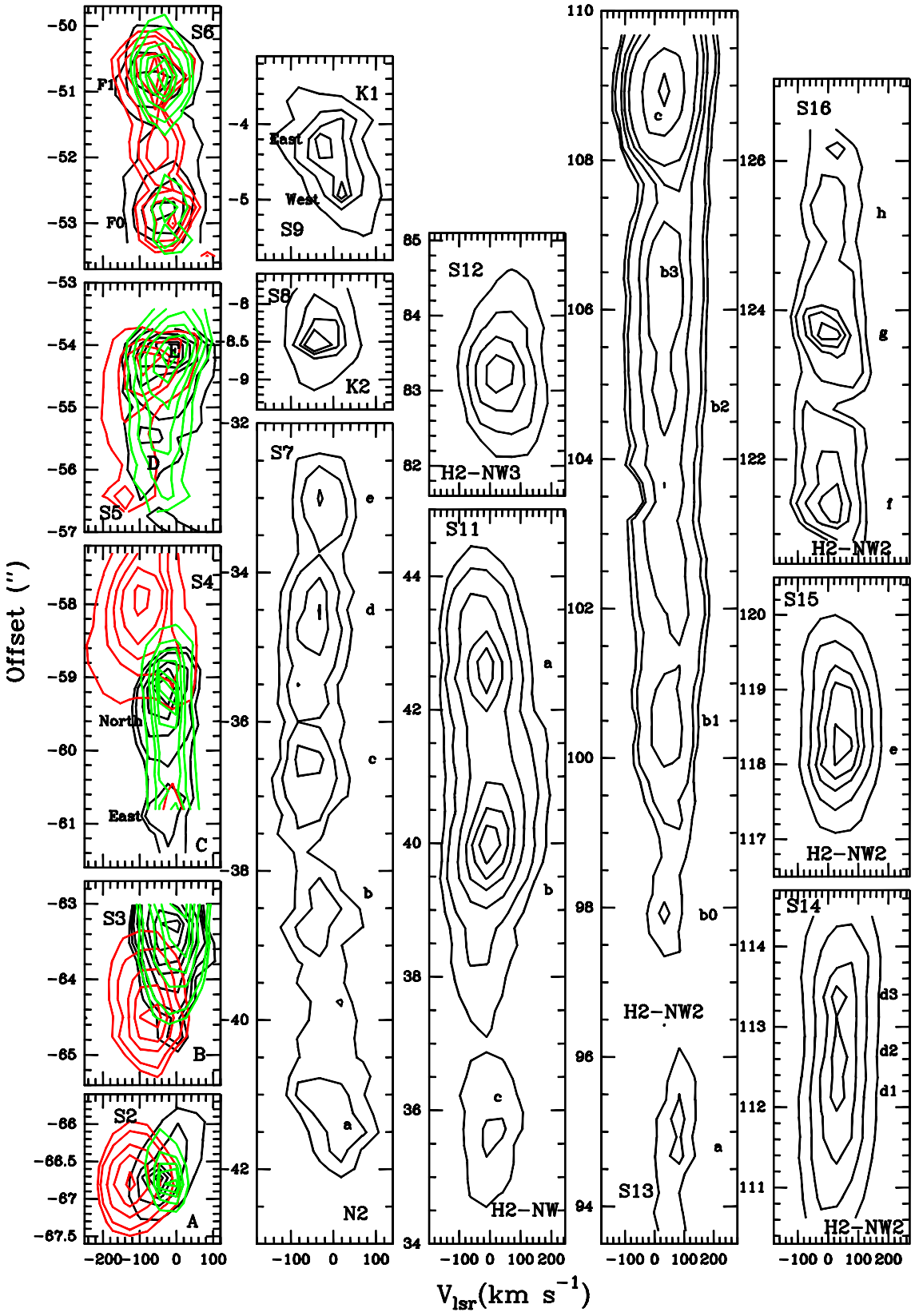

Figure 6. Position-velocity maps of the H_2 2.122 μm line through the slitlet labeled in each panel (black contours). The PV maps of the [Fe II] 1.644 μm are supperposed (red contours) for the slitlets where [Fe II] emission was detected. The PV maps of the H_2 1.748 μm line are also displayed (green contours) for these slitlets to check the reliability of the spatial displacement between the H_2 and [Fe II] emissions. The knots intersected by each slitlet have been labeled to help with the identification.

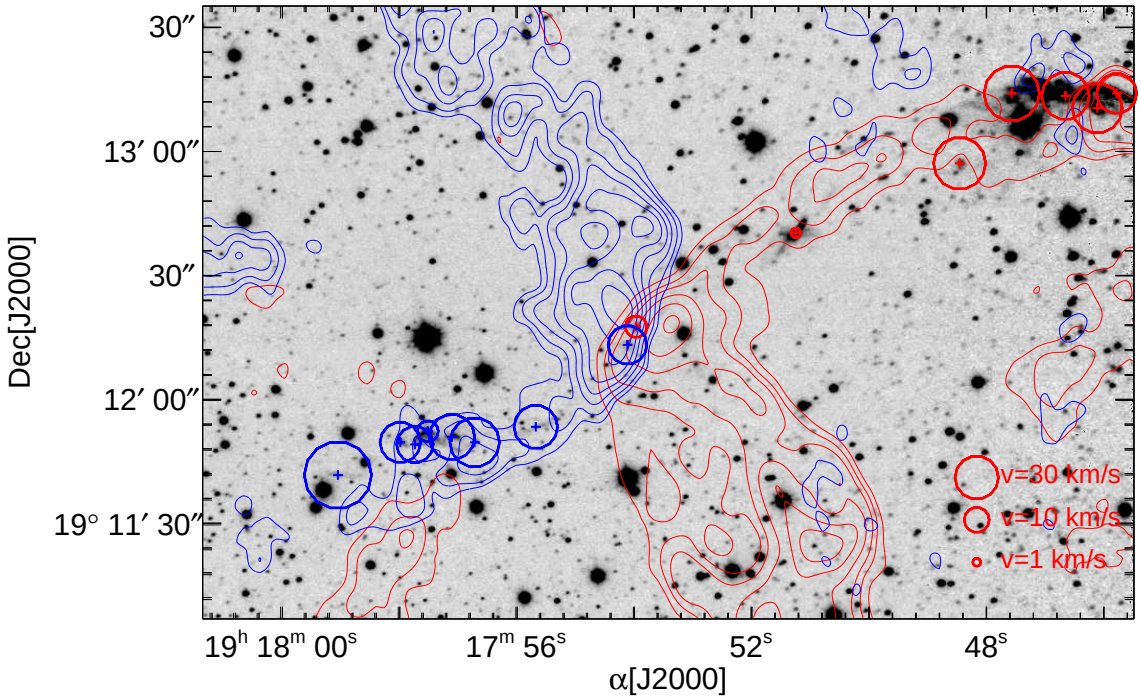

Figure 8. H_2 image of the L723 field (gray scale) supperposed to the contours of the redshifted and blueshifted CO outflows from Lee et al. (2002). The red and blue open circles of different sizes represent the radial velocity obtained from the 2.122 μm line at the knot positions marked by the crosses. (The scale of velocity is shown at the botton right corner).

Table 3. Radial velocities ($V_{\rm LSR}$)[1] of the H_2 2.122 μm emission within the full slitlet aperture

Slitlet	Knot	Offset [2] (arcsec)	$V_{\rm LSR}$ [3] (km s^{-1})
s1	N1	–83.9	-72.1 ± 12.4
s2	A	–67.0	-26.3 ± 9.7
s3	B	–64.0	-21.3 ± 8.2
s4	C	–59.9	-7.0 ± 6.2
s5	D-E	–55.4	-33.2 ± 12.4
s6	F	–51.4	-39.2 ± 14.0
s7	N2	–37.7	-30.3 ± 6.5
s8	K2	–8.3	-24.0 ± 9.8
s9	K1	–3.9	$+7.3 \pm 8.0$
s11	H2-NWab	40.3	$+1.5 \pm 8.3$
s12	H2-NW3	82.8	$+43.3 \pm 11.5$
s13	H2-NW2ab	101.9	$+49.0 \pm 10.6$
s14	H2-NW2d	112.8	$+36.0 \pm 6.1$
s15	H2-NW2e	118.2	$+39.9 \pm 12.6$
s16	H2-NW2fg	123.9	$+25.6 \pm 7.9$

[1] From Gaussian fits to the H_2 2.122 μm line of the spectra, averaged for the full slitlet apertures (see text).
[2] Offsets from the position of SMA 2 to the centre of the slitlet. Typical values of the error are $\leqslant 0.5$ arcsec
[3] The error values correspond to the error of the Gaussian fit added in quadrature with the rms residual of the wavelength calibration.

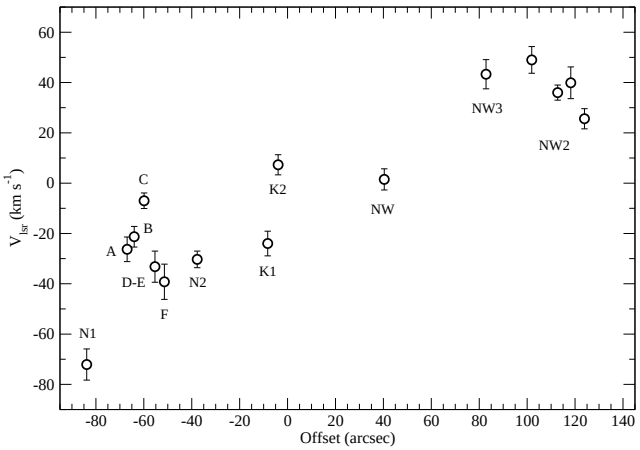

Figure 7. Radial velocities obtained from the line centroid of a Gaussian fits to the H_2 2.122 μm line of the spectra obtained by averaging the signal within the full aperture of the corresponding slitlet. Offsets are relative to the position of SMA 2.

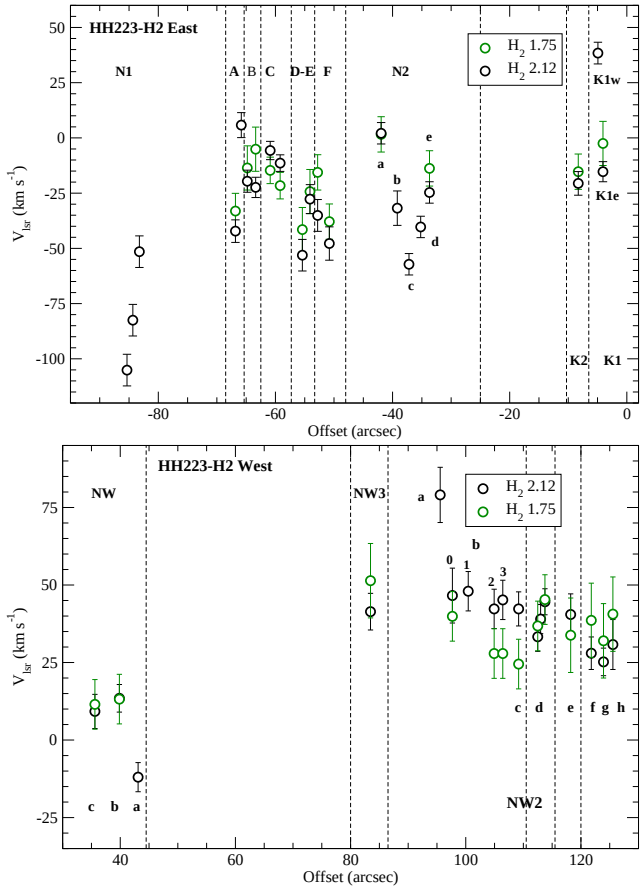

Figure 9. Radial velocities of the identified knots through the slitlets as a function of the distance to SMA 2. Dashed vertical lines are plotted to separate the emission coming from different slitlets.

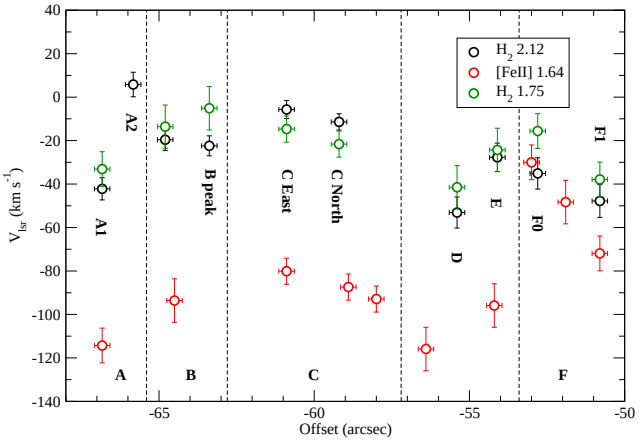

Figure 10. Close-up of Fig. 9 showing the radial velocities of the identified knots through the slitlets covering HH223A-F (the near-infrared counterpart of the HH 223 linear emission feature, detected in Hα and [S II] lines).

3.2.1 *Kinematics of the H_2 emission*

In order to search for a kinematic trend along the HH 223 outflow, we derived the radial velocity[4] from the spectra obtained by averaging the signal within the full aperture of each slitlet (Table 3 and Fig. 7). The velocities derived in this way correspond to the mean velocity within the aperture, and do not account for velocity shifts at spatial scales smaller than the length of the corresponding slitlet, which in some cases covers several knots (see Fig. 6).

The velocities derived in this way are given in Table 3 and Fig. 7 and show a bipolar pattern: the velocity along the outflow changes from negative (blueshifted) in the southwest to positive (redshifted) to the northwest. We found a mean velocity of –32.8 km s^{-1} for the knots observed at distances ranging from 40 to 85 arcsec to the southeast of SMA 2 (the radio-continuum source that hides the outflow exciting source). A mean velocity of +32.5 km s^{-1} is found for the knots located at distances ranging from 40 to 130 arcsec to the northwest of SMA 2. The velocity changes its sign (from negative to positive values) in the neighbourhood of the HH 223-K1 nebula, i. e. close to the position of SMA 2.

It is worth noting that the HH 223 H_2 outflow lies projected onto the pair of lobes of one of the two bipolar CO outflows (the larger, east-west one) detected in L723. As a general trend, the H_2 knots with blueshifted velocities are projected onto the blueshifted CO outflow lobe, while the H_2 knots with redshifted velocities are projected onto the redshifted CO outflow lobe, as can be easily visualized in Fig. 8. This spatial coincidence between the CO and H_2 velocity signs gives support to the existence of a physical relationship between the H_2 and CO outflows.

Furthermore, we searched for changes in velocity at spatial scales smaller than the length of the slitlets. In Fig. 6 (black contours), we plot position-velocity (PV) maps of the H_2 2.122 μm emission through all the slitlets. From these maps, and comparing with the H_2 *K* narrow-band continuum-subtracted image of the field (see López et al. 2010), we identified which knots were intersected by each slitlet. Then, we obtained the one-dimensional spectrum of each of these knots by averaging the signal over the length of the slitlet encompasing the corresponding knot (i. e. within windows 1 arcsec wide and lengths given in Table 4, column 3), and derived the velocity of the knots (Table 4, column 5). The distance, measured as the offset from the position of SMA 2 to the emission peak of the knot, is also given in Table 4. The velocities obtained for the knots projected onto the blue/red lobes of the east-west CO outflow are plotted in Fig. 9 (black dots). These radial velocities will be used later to derive the full spatial velocity field of the near-infrared HH 223 outflow. At small scales we found a rather complex kinematics within the extended nebular emission features, which confirms the previous IFS results (López et al. 2012) for the HH 223 optical counterpart. Note in addition that we detected some additional H_2 features from the MOS spectra that were not detected in the previous H_2 narrow-band image.

Finally, and in order to get further evidence of the kinematic pattern found from the H_2 2.122 μm line, we obtained the velocity of the knots from the 1.748 μm line, the brightest H_2 line detected in most of the *H*-band spectra. The results are shown in Figs. 9 and 10 (green dots). As can be seen from the figures, they are in good agreement with the results found from the H_2 *K*-band line. Concerning the values of the radial velocities, they are consistent with those derived from the 2.122 μm line. Concerning the spatial brightness distribution, the knot structures found from the 2.122 μm line are also identified in the *H*-band maps, and the positions of the peaks of the two H_2 emission lines are coincident. However, the general trend found in all the condensations is that the emission of the 1.748 μm line is detected within a narrower

[4] All the velocities in the paper are given with respect to the velocity adopted for the parent cloud, $V_{\rm LSR}$=+10.9 km s^{-1}(Torrelles et al. 1986)

Table 4. Radial velocities ($V_{\rm LSR}$)[1] of the H_2 2.122 μm emission for the knots identified within the slitlets

Slitlet	Knot HH 223-	Length[2] (arcsec)	Offset [3] (arcsec)	$V_{\rm LSR}$[4] (km s^{-1})
s1	N1			
	N1a	1.00	-85.4	-105.1 ± 14.3
	N1b	0.75	-84.4	-82.5 ± 14.3
	N1c	1.50	-83.2	-51.5 ± 14.3
s2	A			
	A1	1.00	-66.8	-42.2 ± 10.2
	A2	0.75	-65.8	$+5.8 \pm 11.3$
s3	B			
	B-East	1.00	-65.1	-19.6 ± 10.0
	B-peak	1.00	-63.4	-22.4 ± 9.2
s4	C			
	C-East	1.00	-60.9	-5.7 ± 8.3
	C-North	1.50	-59.0	-11.4 ± 7.5
s5	D-E			
	D	1.00	-55.5	-53.1 ± 14.3
	E	1.50	-54.2	-27.7 ± 13.1
s6	F			
	F0	1.50	-52.7	-35.1 ± 14.4
	F1	1.75	-50.9	-47.8 ± 15.1
s7	N2			
	N2a	2.00	-42.0	$+2.1 \pm 9.7$
	N2b	1.75	-39.2	-31.8 ± 15.6
	N2c	2.00	-37.2	-57.2 ± 9.7
	N2d	1.75	-35.2	-40.3 ± 9.7
	N2e	1.00	-33.7	-24.7 ± 9.7
s8	K2			
	K2-peak	1.00	-8.3	-20.6 ± 10.7
s9	K1			
	K1-East	1.25	-4.9	$+38.4 \pm 9.8$
	K1-West	1.00	-4.1	-15.3 ± 9.1
s11	H2-NW			
	H2-NWc	2.75	35.6	$+9.2 \pm 11.0$
	H2-NWb	2.75	39.8	$+13.5 \pm 8.9$
	H2-NWa	3.0	43.1	-12.0 ± 9.4
s12	H2-NW3			
	H2-NW3pe	1.75	83.5	$+41.4 \pm 11.8$
s13	H2-NW2			
	H2-NW2a	1.00	95.6	$+79.1 \pm 17.7$
	H2-NW2b0	1.25	97.7	$+46.6 \pm 17.7$
	H2-NW2b1	1.75	100.4	$+48.0 \pm 12.7$
	H2-NW2b2	1.25	104.9	$+42.3 \pm 12.7$
	H2-NW2b3	2.00	106.4	$+45.2 \pm 12.7$
	H2-NW2c	2.00	109.2	$+42.3 \pm 11.0$
s14	H2-NW2			
	H2-NW2d1	0.75	112.5	$+33.3 \pm 9.4$
	H2-NW2d2	0.75	113.0	$+39.0 \pm 9.4$
	H2-NW2d3	1.00	113.8	$+44.6 \pm 8.4$
s15	H2-NW2			
	H2-NW2e	2.25	118.2	$+40.5 \pm 13.3$
s16	H2-NW2			
	H2-NW2f	1.75	121.8	$+28.0 \pm 10.5$
	H2-NW2g	1.50	123.9	$+25.2 \pm 8.9$
	H2-NW2h	1.00	125.5	$+30.8 \pm 16.1$

[1] From Gaussian fits to the H_2 2.122 μm line of the spectra averaged within apertures of 1 arcsec width and lengths given in column 3.
[2] Length along the slitlet of 1 arcsec width, including emission from the knot.
[3] Offsets from the position of SMA 2 to the centre of the apertures. Typical values of the error are $\leqslant$ 0.5 arcsec
[4] Errors, derived as in Table 3.

Table 5. Radial velocities ($V_{\rm LSR}$)[1] of the [Fe II] 1.644 μm emission for the knots identified within the slitlets

Slitlet	Knot HH 223-	Length[2] (arcsec)	Offset [3] (arcsec)	$V_{\rm LSR}$ [4] (km s^{-1})
s2	A			
	A1	2.75	-66.8	-114.3 ± 10.8
s3	B			
	B-peak	1.00	-64.5	-93.6 ± 9.6
s4	C			
	C-East	1.25	-60.9	-80.1 ± 11.3
	C-North	1.50	-58.9	-87.4 ± 9.5
	C-peak	2.25	-58.0	-92.9 ± 8.5
s5	D-E			
	D	1.25	-56.4	-115.9 ± 13.1
	E	2.00	-54.2	-95.9 ± 12.3
s6	F			
	F0	1.25	-53.0	-30.0 ± 13.6
	F1a	0.75	-51.9	-48.3 ± 15.1
	F1b	2.25	-50.8	-71.9 ± 14.1

[1] From Gaussian fits to the [Fe II] 1.644 μm line of the spectra averaged within apertures of 1 arcsec width and lengths given in column 3.
[2] Length along the slitlet of one arcsec width, including emission from the knot.
[3] Offsets from the position of SMA 2 to the centre of the apertures. Typical values of the error is $\leqslant 0.5$ arcsec
[4] Errors, derived as in Table 3.

velocity range (by $\sim$ 40–60 km s^{-1}) than the emission from the 2.122 μm line (at the same SNR levels).

3.2.2 Kinematics of the ionized outflow gas

We derived the kinematics of the ionized gas by obtaining the velocity from the brightest [Fe II] lines in the *J* and *H* bands (i. e. the 1.257 μm and 1.644 μm lines, respectively). The results found are given in Table 5 and are drawn in Fig. 10 (red dots). The [Fe II] $V_{\rm LSR}$ values appear blueshifted, ranging from $\sim$ –30 to $\sim$ –115 km s^{-1}. These velocities show that the ionized gas of the outflow (traced by the [Fe II] emission) is more blueshifted than the molecular gas (traced by the H_2 emission).

3.2.3 Individual outflow features

In the following, we will briefly discuss the kinematic structure found at small scales, by examining each of the nebulae sampled with MOS through all the slitlets.

HH 223-A to HH 223-F

Five slitlets (S2 to S6, from east to west) were positioned covering the knots HH 223-A to F, the knotty, undulating emission of $\sim$ 22 arcsec in length, at $\sim$ 1 arcmin southeast of SMA 2. Note that this structure is the optical counterpart of the Hα "linear emission feature" reported by Vrba et al. (1986), and corresponds to the Herbig-Haro object 223.

Figure 6 (left column) displays the PV maps of the H_2 emission lines at 2.122 μm (black) and 1.748 μm (green), and [Fe II] at 1.644 μm (red) through the S2 to S6 slitlets. The knots intersected by the slitlets, and identified from the H_2 *K*-narrow-band, continuum substracted image of the field, have been labeled accordingly. Figure 10 displays a close-up of Fig. 9 showing with more detail the behaviour of the velocity as a function of the angular distance to SMA 2. The spectrum of each knot was obtained by averaging the signal within the apertures quoted in Table 4, and the velocities were derived from the 1.748 μm and 2.122 μm H_2, and 1.644 μm [Fe II] lines. Both emissions, the neutral (traced by H_2) and the ionized (traced by [Fe II]) appear blueshifted. As expected, the velocities derived from [Fe II] are more blueshifted than those derived for both H_2 lines, which in turn are consistent between them. Accordingly with what was found in the PV maps (see Fig. 6) and in the *H*- and *K*-narrow-band images (López et al. 2010), there is some shift between the spatial distribution of the [Fe II] and H_2 emissions: offset values $\geqslant$ 1 arcsec are found between the peaks of the [Fe II] and H_2 emissions in knots HH 223-B, -C (that corresponds to -C North in H_2), and -D. Furthermore, there are some substructures that were detected in H_2 but did not appear in [Fe II] (e. g. HH 223-A2) while some [Fe II] substructures were not detected in H_2 (e. g. a third condensation lying between HH 223-F0 and -F1). As it was noted, these facts may be indicative of shocks of different degree of excitation coexisting along the HH 223-A to -F emission region.

A trend for the velocity can be found, consisiting in an increase of the absolute value of the velocity, suggestive of an acceleration, from east to west, towards the location of SMA 2. The general trend seems to be broken at a few positions (e. g. at A1 and D knots). However, this might be expected because of the highly complex kinematics of HH 223-A-F already found at optical wavelengths, where a fully spatial sampling of the emission was obtained with Integral Field Spectroscopy (López et al. 2012). One indication of such a highly complex kinematics can be found by examining the PV maps of the 2.122 μm line of HH 223-A-F at spatial scales of $\sim$ 1 arcsec: as can be seen from Fig. 6, a change in velocity can be appreciated along HH 223-A (i. e. in S2). Moving from east to west through the slitlet, we found an intensity peak of emission, labeled as knot HH 223-A1 in Table 4, and another secondary emission enhancement (HH 223-A2 in Table 4), their peaks being separated $\sim$ 1 arcsec. From the spectra obtained for these two HH 223-A knots we found a difference in velocity of $\sim$ 50 km s^{-1} between them, being the eastern knot more blueshifted. It is worth noting that HH 223-A presents two emission peaks separated $\sim$ 1 arcsec, partially resolved in the Hα images (López et al. 2009). The radial velocities derived from the Hα and [S II] lines in long-slit spectra through HH 223-A show the same behaviour as in the case of the H_2 line: a change in velocity of $\sim$ 60 km s^{-1} between these two condensations of HH 223-A, being the eastern condensation (HH 223-A1) the most blueshifted. Furthermore, the velocity trend shown by the 2.122 μm line through HH 223-A is also found in other H_2 lines (e. g. the 2.224 μm and the 2.406 μm). In contrast, the two H_2 substructures found within HH 223-A were not identified in the PV map of the [Fe II] 1.644 μm line. The position of the [Fe II] emission peak coincides with HH 223-A1, while no clear [Fe II] counterpart is found for the other H_2 substructure (HH 223-A2) . Hence, we confirm that there are two unresolved clumps within HH 223-A, with different excitation conditions, which may be originated in shocks with different strengths.

In spite of the lack of detection of H_2 emission from the knot HH 223-B in the narrow-band images, we were able to detect H_2 emission through the slitlet positioned on this knot (S3). From the H_2 2.122 μm line, we derived the velocity at the intensity peak of the emission, and at a secondary weaker substructure lying to its southeast (named HH 223-B-peak and -B-east, respectively; see Table 4). At both positions the emission appears blueshifted, although no significant variation in velocity along the knot is found. In addition, we detected emission from other H_2 lines, both in the *H* and

K bands, the behaviour being consistent with that of the 2.122 μm emission (see e. g. the PV map of the 1.748 μm emission in Fig. 6). Note, in contrast, the spatial displacement found between the [Fe II] and H_2 emissions, inferred from their PV maps (Fig.4). The position of the [Fe II] emission peak is coincident (within 0.2 arcsec) with the peak of HH 223-B-east, the H_2 weaker substructure, but it is offset by 1.4 arcsec from HH 223-B-peak.

The slitlet S4 included emission from the intensity peak of the bow-shaped feature labeled HH 223-C in the narrow-band H_2 image, and from a weaker condensation, southeast of it (labeled HH 223-C-North and C-East, respectively, in this work). A spatial shift between the [Fe II] and H_2 emissions was already found in the *H* and *K* narrow-band images, and also can be appreciated in the PV maps of this work. The peak of the [Fe II] emission is offset by $\sim$ 1.2 arcsec west from the peak of the H_2 emission (HH 223-C-North).

The slitlet S5 included emission coming from the bow-shaped feature HH 223-E, and from HH 223-D. We found an offset of $\sim$ 1 arcsec between the peaks of the [Fe II] and H_2 emissions in HH 223-D, while there is not a significant shift between the peaks of these emissions for HH 223-E. Finally, S6 included the emission from the filamentary feature HH 223-F. The spatial brightness distribution of the ionized ([Fe II]) and neutral (H_2) emissions are in general coincident, although some differences are found. Two condensations, F0 and F1, are identified in the PV map of both, H_2 and [Fe II] emissions, while the [Fe II] emission presents a third condensation located between them. The trend of decreasing velocity from east to west is seen through HH 223-F for both ionized and neutral emissions.

HH 223-N2

The slitlet S7 was positioned along the H_2 faint filamentary structure $\sim$ 30 arcsec northwest of HH 223-A. We identified several brightness enhancements that were detected only in the brighter H_2 lines (e. g. 1.748 μm and 2.122 μm). In contrast, emission from [Fe II] was not detected in the spectral range observed. No clear trend along the filament for the radial velocity was found. On the other hand, the tangential velocity cannot be derived from the narrow-band images due to the low contrast brightness distribution of the clumps. Hence, it is not possible to infer whether the observed kinematics could be tracing some changes in the outflow orientation at this region.

HH 223-K2, –K1

Two slitlets were positioned on the H_2 nebulae closest to the location of SMA 2. The H_2 emission from HH 223-K2 (through S8) appears blueshifted, without significant velocity variations along the region mapped. In contrast, the velocity derived along S9 shows some variation from east (blueshifted) to west (redshifted). Note that S9 was positioned closely perpendicular to HH 223-K1. Hence, the K1-West emission peak is the closest emission to the wall of the cavity opened by the CO outflow. In spite of these slitlets being the closest to the YSO position, we were not able to detect emission from [Fe II] lines.

HH 223-H2-NW

Slitlet S11 sampled the emission along the filamentary feature HH 223-H2-NW, crossing the two bright knots (labeled NWa and NWb, from west to east), and the weaker, diffuse emission labeled NWc. From the 2.122 μm line, we derived similar redshifted velocity values for knots NWc and NWb, as expected for the H_2 knots lying projected onto the redshifted CO outflow lobe. In contrast, a blueshifted velocity was derived at NWa. At the brighter knots (NWa and NWb), emission from other H_2 lines of the *K*-band was also detected. Thus, in addition to the 2.122 μm line, we used the 2.224 μm and 2.248 μm lines for deriving their velocities. From these three lines, we found mean velocities of +13.3 $\pm$ 0.2 km s^{-1} and –12.0 $\pm$ 0.9 km s^{-1} for knots NWb and NWa respectively. Then, we concluded that this difference in velocity between knots a and b, c is reliable.

HH 223-H2-NW3

Slitlet S12 was positioned on this isolated, compact ($\sim$ 2 arcsec in diameter) emission feature, seen in the narrow-band images towards the southeast of the filamentary feature HH 223-H2-NW2. We were not able to identify substructures within the knot. The velocity of the knot is redshifted, without significant variations along it.

HH 223-H2-NW2

This bright H_2 filamentary feature is seen towards the northwestern edge of the observed field. Part of it coincides with the *K'* linear nebula reported by Hodapp (1994), and has a faint, less extended optical counterpart visible in the Hα line (López et al. 2006). The filament appeared resolved in several brightness enhancements, labeled *a* to *g*, in the narrow-band H_2 images (López et al. 2010).

Up to four slitlets (S13 to S16) were positioned along this filament in order to cover the emission coming from most of its bright knots. S13 included emission from a part of the faint, more extended nebula NW2a, the eastern part of the filament, from NW2b, which was resolved into several smaller-scale emission enhancements (labeled b0 to b3, from east to west along the filament), and most of the NW2c knot. S14 included emission from NW2d, which showed three emission enhancements (labeled d1 to d3, from east to west along the feature). S15 crossed NW2e, which showed a compact, single-peaked emission in all the detected H_2 lines. Finally, S16 included emission coming from NW2f, NW2g, and from NW2h, a more difuse, fainter emission, first identified from MOS spectra.

Using the 2.122 μm line, we derived the velocity for each of the condensations identified in the MOS spectra. The general trend shows a slight decrease of the redshifted velocity, which diminished by a factor of $\sim$ 2 in $\sim$ 25 arcsec along the filament, from east to west.

3.3 Proper motions

The proper motions of the knots along the HH 223 outflow were derived from three H_2 narrow-band images of the L723 field obtained at three differents epochs, spanning a total of 6 years (see Table 1).

The three images were converted into a common reference system. The positions of ten field stars, common to all the frames, were used to register the images. The *geomap* and *geotran* tasks of IRAF were applied to perform a linear transformation, with six free parameters that take into account translation, rotation and magnification between different frames. After the transformation, the typical rms of the difference in position for the reference stars between the reference epoch and the other two epochs was $\sim$ 0.03 arcsec in both coordinates. The pixel size was found to be 0.252 arcsec.

We defined boxes that included the emission of the individual condensations in each epoch. The position offset of the second and third epochs with respect to the first epoch (taken as reference) was estimated by cross-correlation (see the description of this method in Reipurth et al. 1992; López et al. 1996). The uncertainty in the position of the correlation peak was estimated in the same way as was done by Anglada et al. (2007), through the scatter of the correlation peak positions obtained from boxes differing from the nominal one in $\pm$2 pixels. The error adopted for each coordinate for the offset

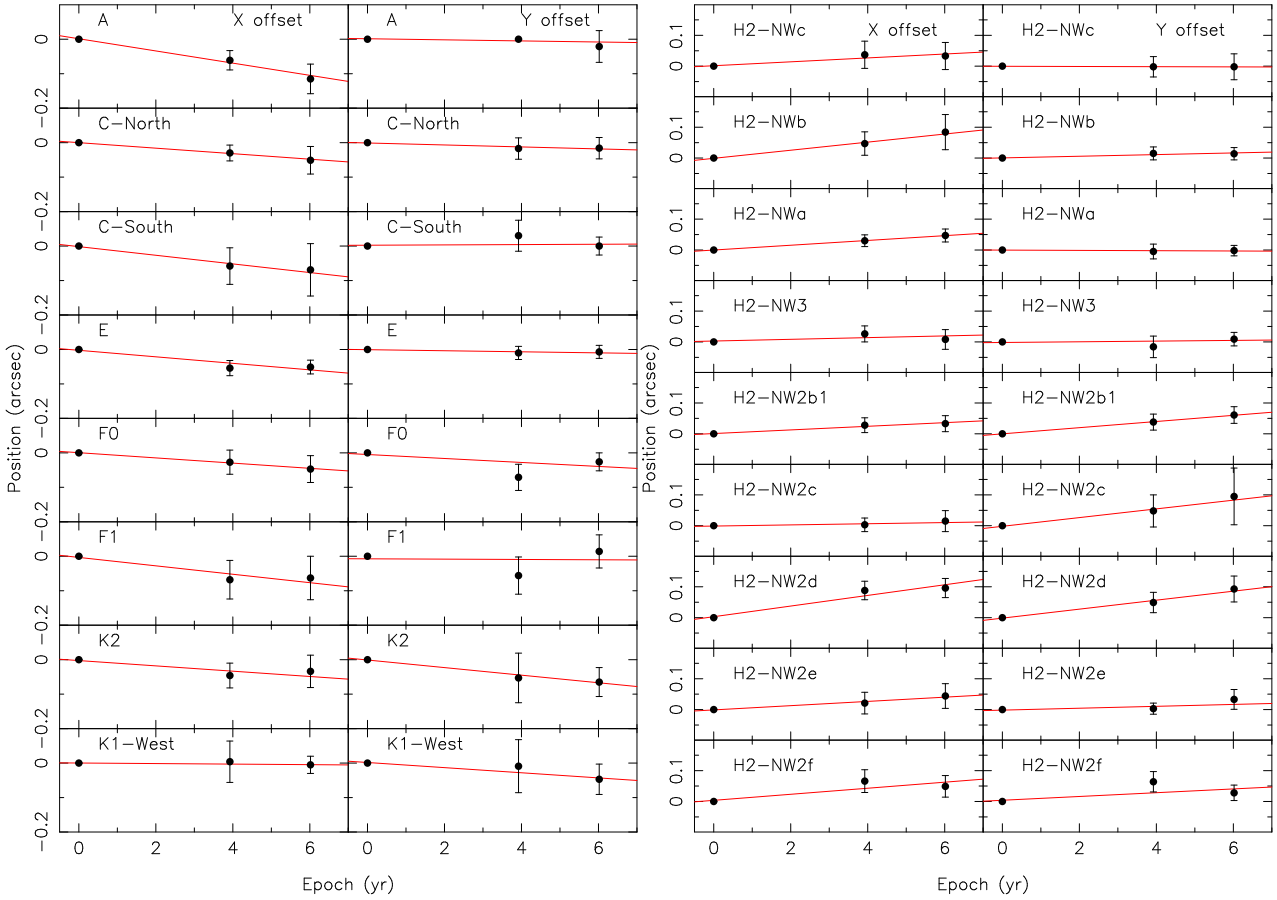

Figure 11. Proper motions derived for the HH 223 knots labeleled in the panels. For each epoch, a circle represents the displacements (in arcsec) in the x-direction (left) and y-direction (right) of the corresponding knot measured from the first-epoch image, which defines the origin of the time-scale (set on 2006 July 20). Errors are indicated by vertical bars. The least-squared fits derived for the displacements of each knot are shown by the red lines. The proper motion of the knots in the x and y direction are derived from the slopes of these lines.

Table 6. Positions and Proper Motions of H_2 Knots

Knot HH 223-	x^a (arcsec)	y^a (arcsec)	$\mu_x{}^b$ (arcsec yr^{-1})	$\mu_y{}^b$ (arcsec yr^{-1})	$\epsilon_x{}^c$ (arcsec)	$\epsilon_y{}^c$ (arcsec)	$V_T{}^d$ (km s^{-1})	PA (deg)
A	−60.6	−29.8	-0.0177 ± 0.0014	-0.0015 ± 0.0015	0.0059	0.0057	25.3 ± 2.0	95 ± 5
C-North	−54.2	−27.0	-0.0080 ± 0.0003	-0.0029 ± 0.0006	0.0012	0.0027	12.2 ± 0.5	110 ± 4
C-South	−52.4	−29.2	-0.0126 ± 0.0013	0.0005 ± 0.0020	0.0053	0.0097	17.9 ± 1.8	88 ± 9
E	−47.3	−28.2	-0.0094 ± 0.0018	-0.0015 ± 0.0005	0.0081	0.0022	13.5 ± 2.5	99 ± 3
F0	−46.4	−31.6	-0.0076 ± 0.0003	-0.0057 ± 0.0040	0.0014	0.0192	13.5 ± 3.5	127 ± 19
F1	−43.0	−29.9	-0.0122 ± 0.0026	-0.0005 ± 0.0057	0.0114	0.0261	17.4 ± 3.7	92 ± 27
K2	−5.5	−5.9	-0.0076 ± 0.0024	-0.0110 ± 0.0007	0.0100	0.0036	19.0 ± 2.1	145 ± 8
K1-West	−3.4	−1.6	-0.0008 ± 0.0004	-0.0075 ± 0.0015	0.0020	0.0071	10.7 ± 2.1	174 ± 3
H2-NWc	31.7	16.5	0.0063 ± 0.0014	-0.0003 ± 0.0001	0.0062	0.0002	9.0 ± 1.9	-93 ± 1
H2-NWb	34.5	20.3	0.0131 ± 0.0008	0.0026 ± 0.0005	0.0032	0.0023	19.1 ± 1.1	-79 ± 2
H2-NWa	36.3	22.5	0.0078 ± 0.0001	-0.0005 ± 0.0003	0.0001	0.0012	11.1 ± 0.1	-94 ± 2
H2-NW3	74.7	37.7	0.0098 ± 0.0031	0.0061 ± 0.0036	0.0140	0.0171	16.4 ± 4.6	-58 ± 17
H2-NW2b1	86.7	52.9	0.0028 ± 0.0021	0.0011 ± 0.0016	0.0089	0.0076	4.3 ± 2.8	-69 ± 31
H2-NW2c	94.7	56.3	0.0059 ± 0.0006	0.0101 ± 0.0002	0.0028	0.0008	16.7 ± 0.5	-31 ± 3
H2-NW2d	98.0	54.1	0.0018 ± 0.0007	0.0141 ± 0.0014	0.0028	0.0056	20.2 ± 2.0	-7 ± 3
H2-NW2e	107.5	51.2	0.0173 ± 0.0023	0.0145 ± 0.0011	0.0104	0.0048	32.1 ± 2.7	-50 ± 4
H2-NW2f	107.5	56.2	0.0068 ± 0.0007	0.0031 ± 0.0019	0.0032	0.0074	10.7 ± 1.5	-65 ± 13

[a] Offsets from the position of SMA 2, $\alpha(J2000) = 19^{\rm h}17^{\rm m}53\overset{\rm s}{.}694$, $\delta(J2000) = 19^\circ12'19\overset{''}{.}68$, of the intensity peak in the 2006 image. For the more extended knots, Cs and H2NW2f+g, the position of the center of the box used for the proper motion determination is given. The x axis points westwards, and the y axis northwards. [b] Error values are the error in the proper motion fit to the three epochs observed. [c] rms residual of the knot positions in the proper motion fit, $\epsilon = \sigma\sqrt{1-r^2}$, where σ is the standard deviation and r is the correlation coefficient. [d] Proper motion velocity, assuming a distance of 300 pc.

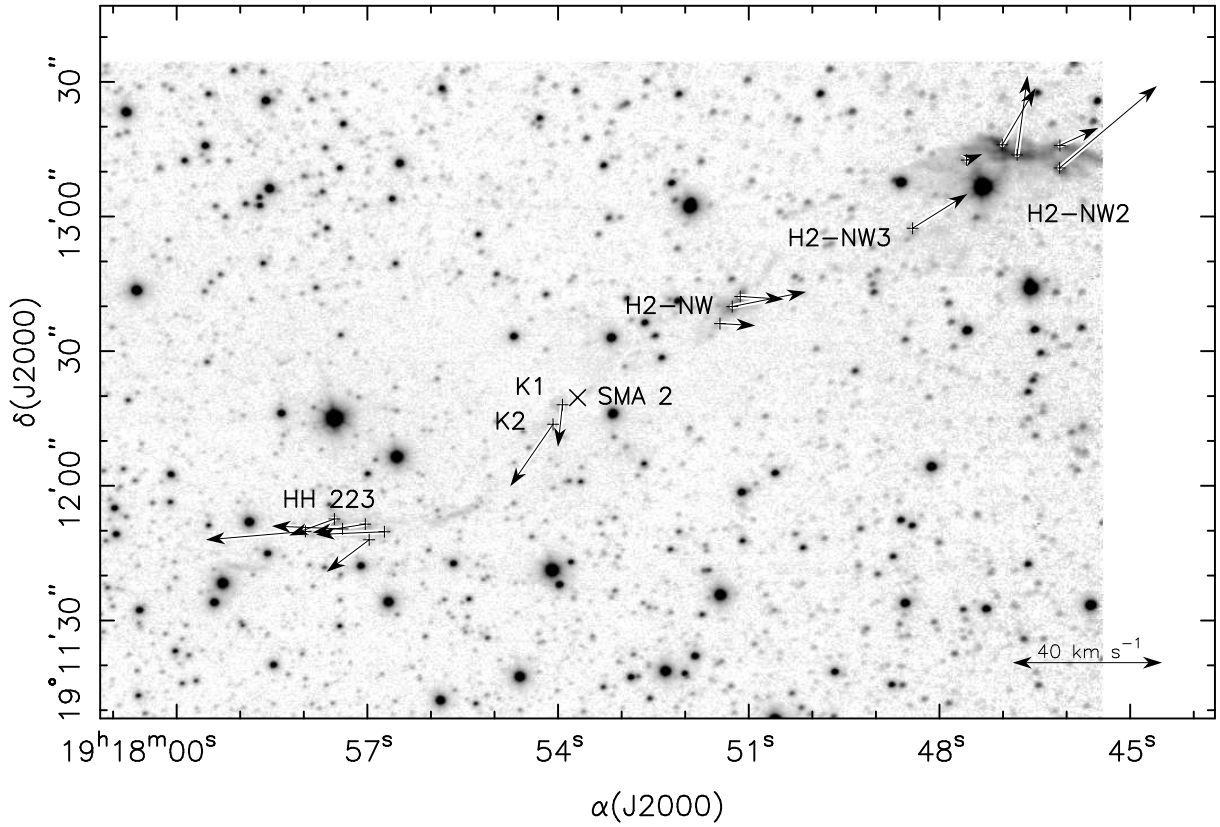

Figure 12. Image of the L723 field through the H_2 2.122 μm line filter (continuum is not subtracted). The arrows indicate the proper motion velocity (V_T) derived for each knot. The position of SMA 2 is indicated by a $\times$ sign. The scale of the arrows (in km s^{-1}) is indicated by the double headed arrow at the bottom right corner of the map.

for epoch i, ϵ_i, was twice the uncertainty in the correlation peak position, added quadratically to the rms alignment error.

In Fig. 11 we show the position offsets in x and y measured for the knots. The proper motions in the x and y direction, μ_x and μ_y, were obtained for each knot as the slope of the regression lines fitted to the offset positions for the three epochs (see Fig. 11). The proper motions obtained are shown in Table 6 and in Fig. 12. The errors assigned to the proper motions, in both x and y, are the formal errors of the slope of the linear regression fits for each knot. The errors appear to be rather small as a consequence of the wide time span used for calculating the proper motions. The quality of the linear regression fits for each knot is indicated by the small values of the residuals in x, ϵ_x, and y, ϵ_y, (see Table 6).

As can be seen in Table 6 and Fig. 12, the pattern found for the tangential velocity (V_T) is symmetric with respect to the location of the proposed outflow source, which is located close to the knot HH 223-K1.

The V_T derived are quite similar for both (blue- and redshifted) outflow lobes. For the knots located on the blueshifted CO outflow lobe (i. e. to the east of the millimetre sources) V_T ranges from $\sim$ 11 to 25 km s^{-1} with a mean velocity of 15.9 km s^{-1}. For the knots on the redshifted CO outflow lobe (to the west of the millimetre sources) V_T ranges from $\sim$ 4 to 32 km s^{-1} with a mean velocity of 15.5 km s^{-1}.

Zhang et al. (2013) carry out a survey of H_2 outflows driven by low-mass protostars in the L1688 core of ρ Ophiuchi, and derive the proper motions for 86 H_2 emission features. They find values in the range of 0.014–0.247 arcsec yr^{-1}, which correspond to V_T in the range of 8–140 km s^{-1}, with a median velocity of 34.5 km s^{-1}. The proper motions we measured for the H_2 features of the HH 223 outflow lie within this range, near its lower end. It should be noted that these authors also find an appreciable drop in the number of features having low V_T values, which they mainly attribute to a bias effect. Thus, the V_T we derived for the H_2 features of the HH 223 outflow are consistent with typical values found in other H_2 outflows driven by low-mass protostars.

Regarding the direction of the knot proper motions, the position angles (PA) derived show that the knots located to the east of SMA 2 move eastwards, in a direction opposite to that of the knots located to the west of SMA 2, which move westwards. In general, the knot proper motions are projected following directions that are consistent, within errors, with the direction of the east-west CO outflow axis (PA of 110–115°, see e. g. Moriarty-Schieven & Snell 1989; Lee et al. 2002), with a few exceptions. The knots closest ($\leqslant$ 10 arcsec east) to SMA 2 (HH 223-K1 and -K2) also move eastwards but the PA of their proper motions are misaligned with respect to the large-scale outflow axis (Δ PA 30°– 65°). However, at small scales, the ouflow traced by the SiO emission has a PA close to that of the H_2 emission of knots K1 and K2 (see Girart, Rao & Estalella 2009; López et al. 2010). The proper motion of the knots H2-NW2c and H2-NW2d, $\sim$ 95 arcsec to the west of the millimetre sources, are also misaligned with respect to the east-west CO outflow axis. The CO velocity maps of Lee et al. (2002) show the presence of a clump of blueshifted CO emission, superposed on the redshifted CO outlfow lobe, around the location of these H_2 knots. It might be indicative of a complex interaction between molecular clumps at these positions that deviates the knot proper motions away from the outflow axis. Such deviations, at-

Table 7. Full spatial velocities ($V_{\rm tot}$) and inclination angle (ϕ)[1]

Knot HH 223-	$V_{\rm tot}$ (km s^{-1})	ϕ (degrees)
A1	49.2 ± 10.4	59 ± 8
C-North	16.7 ± 7.5	43 ± 25
E	30.8 ± 13.3	64 ± 19
F0	37.6 ± 15.0	69 ± 16
F1	50.9 ± 15.6	70 ± 10
K2	28.0 ± 10.9	47 ± 20
K1-West	18.7 ± 9.3	55 ± 27
H2-NWc	12.9 ± 11.2	-46 ± 20
H2-NWb	23.4 ± 9.0	-35 ± 14
H2-NWa	16.3 ± 9.4	47 ± 34
H2-NW3	44.5 ± 12.7	-68 ± 12
H2-NW2b	48.2 ± 12.0	-85 ± 4
H2-NW2c	45.5 ± 11.0	-68 ± 8
H2-NW2d	38.9 ± 9.6	-59 ± 12
H2-NW2e	51.7 ± 13.6	-52 ± 15
H2-NW2f	30.0 ± 10.6	-69 ± 12

[1] Angle between the knot velocity and the plane of the sky, positive towards the observer.

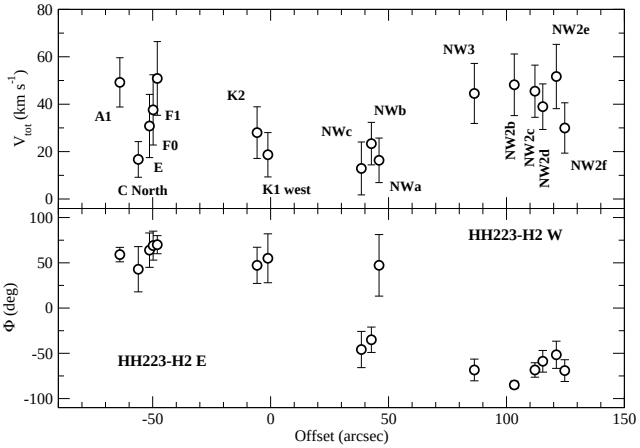

Figure 13. Full spatial velocity ($V_{\rm tot}$) and angle (ϕ) between the knot velocity and the sky plane (with $\phi \geqslant 0$ towards the observer)

tributed to complex interactions of the outflow with a inhomogeneous environment, have been observed in other jets (e. g. HH 110, see Kajdic et al. 2012).

3.4 Full spatial velocities

The full spatial velocity ($V_{\rm tot}$) and the angle (ϕ) between the knot motion and the sky (with $\phi \geqslant 0$ towards the observer) was obtained for the knots for which the two velocity components could be derived from the MOS and narrow-band imaging observations. Results are given in Table 7 and plotted in Fig. 13.

The full spatial velocities derived for these knots range from $\sim$ 15 to 55 km s^{-1}. No clear behaviour as a function of the distance to SMA 2 is found. However, a trend can be seen, with $V_{\rm tot}$ increasing with distance from the exciting source. Near SMA 2, the knots lying from $\sim$ –5 to +40 arcsec of SMA 2 have lower $V_{\rm tot}$(with a mean velocity of 17.8 km s^{-1}) than the knots far away of SMA 2, to both sides of it. Furthermore, $V_{\rm tot}$ is slightly higher for the western (redshifted) knots lying at distances from +80 to +120 arcsec, (with a mean velocity of 43 km s^{-1}), than for the eastern (blueshifted) knots lying at distances from –10 to –70 arcsec to SMA 2 (with a mean velocity of 35.5 km s^{-1}).

In contrast, the inclination angle with respect to the plane of the sky derived for the knot motions shows a bipolar behaviour, as can be appreciated in Fig. 13. For the knots located to the east of SMA 2, we derived inclination angles $\geqslant 50^\circ$, with a mean inclination angle of 58°. The motion of the knots lying to the west of SMA 2 is found projected in the opposite direction with respect to the plane of the sky, with a mean inclination angle of –60°.

3.5 A scenario derived from the kinematics

A scenario was previously outlined by López et al. (2010), which was based only on the morphology of the near-infrared and CO outflows, with the low-mass protobinary system VLA 2 lying embedded in the millimetre source SMA 2. One of the protobinary members (most probably VLA 2A) is ejecting supersonic gas at varying speed or with different ejection directions, giving rise to the large-scale, east-west bipolar CO outflow. In turn, the near-infrared HH 223 outflow is tracing slow shocks, excited by the interaction of the CO outflow with the accelerated gas of the walls of the cavity opened by it. At some places, the strength of the shocks increases, either by interaction between parcels of the outflow (internal working surfaces) or with dense clumps of the cavity wall. These sites of stronger shocks are traced by the [Fe II] emission in the *J* and *H* spectral range, provided that the extinction allows the emission to emerge. The near-infrared emission arising from the shocked gas has, in addition, optical counterparts at the regions with low visual extinction, giving rise to the Herbig-Haro object 223, at the southeast edge of the outflow, and to the weak, diffuse HH 223-NW2 filament at its northwest edge, both structures being detected in the Hα line.

In this work, the full kinematics derived for the H_2 emission clearly confirms that the location of the exciting outflow source has to be found around the position of the millimetre source SMA 2, where the protobinary system is embedded. A bipolar pattern has been found for the spatial distribution of the knots' proper-motion directions, as well as for the inclination angle of the full velocity with respect to the plane of sky. In both cases, the vectors point in opposite direction, away from the region where the proposed engine of the outflow is located. Furthermore, the radial velocity derived along the near-infrared emission sampled with MOS changes sign somewhere to the northwest of HH 223-K1. Note that the location of the proposed engine of the outflow lies a few arcsec to the northwest of HH 223-K1. Unfortunately the high extinction prevented us to detect near-infrared emission just coinciding with the position of the millimetre source SMA 2. Hence, from this work it is not possible to establish which component of the protobinary system is closer to the location where the velocity changes sign. To address this subject, we would need to study the kinematics of the emission in the neibourghood of HH 223-K1 using tracers of the emission from dense gas that would allow us to penetrate closer to the millimetre source.

Finally, we found some departures from the general trend followed by the kinematics of the near-infrared emission at several positions. We interpreted them as caused by a more complex interaction with an inhomogeneous, clumpy environment or between different parcels of the outflow.

4 SUMMARY AND CONCLUSIONS

Taking advantadge of the Multi-Object-Spectroscopy (MOS) observing mode of LIRIS, we obtained *J*, *H* and *K*-band spectroscopy of the complex morphology of the L723 outflow. We obtained the full kinematics of the near-infrared (H_2) outflow HH 223, located in the L723 dark cloud. The proper motions were derived from multi-epoch H_2 images of the L723 field, obtained through a narrow-band filter centred on the 2.122 μm line. The radial velocities were derived from the 2.122 μm H_2 lines of the MOS spectra. Hence, both radial and tangential velocities correspond to the same emitting outflow gas. The kinematics derived from the data presented in this work lead us to the conclusions summarized below.

- At large scales, the radial velocity shows a bipolar pattern along the outflow, with negative (blueshifted) values towards the southeast, and positive (redshifted) values towards the northwest from the position of SMA 2. The spatial distributions of the radial velocity of the H_2 and CO emissions match each other: the H_2 knots having negative velocity lie on the blueshifted CO lobe, while the H_2 knots with positive velocity lie on the redshifted CO lobe. This strongly supports that the H_2 and CO outflows share their exciting source.
- The proper motions derived lie within the range of values found in other H_2 outflows driven by low-mass protostars. The proper motions of the blueshifted and of the redshifted H_2 knots have similar values. As a general trend, the knots move following the direction of the CO outflow axis. The proper motions follow a bipolar pattern, with the knots to the east of SMA 2 moving in a direction opposite to the motions of the knots to the west of SMA 2.
- For the brightest H_2 knots, we derived the full spatial velocity and the inclination angle of their motion with respect to the plane of the sky. A bipolar pattern, centred around the location of SMA 2 (where the exciting outflow source is embbeded), is found: the eastern knots move towards the observer ($\phi \simeq +60^\circ$), while the western knots move far away to the observer ($\phi \simeq -60^\circ$).
- In addition, we built the PV maps of the 1.748 μm line, the brightest H_2 line detected in the observed *H*- spectral range, and derived the radial velocity from this line. Both, radial velocities and spatial brightness distribution are consistent with those derived from the 2.122 μm line.
- Emission from [Fe II] lines, tracing the emission of the ionized gas, was only detected in the *J*- and *H*- band spectra of the slitlets positioned on HH 223-A to HH 223-F. Since these knots are far away from the location of the powering outflow source, the [Fe II] emission has to be originated in shocks.

In summary, the 3D kinematics of the HH 223 H_2 outflow derived in this work confirms that all the H_2 nebular structures form part of a large-scale, S-shaped near-infrared outflow, which is powered by the YSO located within the millimetre source SMA 2, the closest one to the H_2 knot HH 223-K1. The kinematics also confirms that the H_2 and CO outflows are physically related.

ACKNOWLEDGMENTS

The paper is based on observations made with the 4.2 m William Herschel Telescope operated on the island of La Palma by the ING at the Observatorio del Roque de los Muchachos of the Instituto de Astrofísica de Canarias.
J. A-P. is partially supported by AYA2011-25527. B. G.-L. acknowledges finantial support from the Spanish MINECO grants AYA2012-39408-C0-02 and AYA2013-41656-P. R. E. and R. L. are partially supported by the Spanish MICINN grant AYA2011-30228-C03-03. R. L. akcnowledges the hospitality of the Instituto de Astrofísica de Canarias, where part of this work was done.
We thanks the referee, Prof. A. Raga, for the detailed revision of the manuscript.

REFERENCES

Acosta-Pulido, J. A., et al. 2003, The Newsletter of the Isaac Newton Group of Telescopes, 7, 15.
Anglada, G., Rodríguez, L.F., & Torrelles, J.M. 1996, ApJ, 473, L123.
Anglada, G., López, R., Estalella, R., Masegosa, J., Riera, A., & Raga, A.C. 2007, AJ, 132, 2799.
Carrasco-González, C., Anglada, G., Rodríguez, L. F., Torrelles, J. M., Osorio, M., & Girart, J. M. 2008, ApJ, 676, 1073
Davies R. I., 2007, MNRAS, 375, 1099
Girart, J. M., Rao, R., & Estalella, R. 2009, ApJ, 694, 56
Goldsmith, P. F., Snell, R. L., Hemeon-Heyer, M., & Langer, W. D. 1984, ApJ, 286, 599.
Hoddap, K.-W. 1994, ApJS, 94, 615.
Kajdic, P., Reipurth, B., Raga, A.C., Bally, J., & Walawender, J. 2012, AJ, 143, 106.
Lee, C.F., Mundy, L.G., Stone, J.M., & Ostriker, E.C. 2002, ApJ, 576, 294.
López, R., Estalella, R., Gómez, G., & Riera, A. 2006, A&A, 454, 233.
López, R., Estalella, R., Gómez, G., Riera, A., & Carrasco-González, C, 2009,A&A, 498, 761.
López, R., Riera, A., Raga, A. C., Anglada, G., López, J. A., Noriega-Crespo, A., Estalella, R., 1996, MNRAS, 282, 470.
López, R., Acosta-Pulido, J. A., Estalella, R., Gómez, G. & Carrasco-González, C. 2010, A&A, 523, A16.
López, R., García-Lorenzo, B., Estalella, R., Riera, A., Carrasco-González, C., & Gómez, G. 2012, MNRAS, 424, 1817.
Manchado A., et al., 2004, SPIE, 5492, 1094.
Moriarty-Schieven, G.H. & Snell, R. 1989, ApJ, 338, 952.
Palacios, J. & Eiroa, C. 1999, A&A, 346, 233.
Reipurth, B., Raga, A. C., Heathcote, S., 1992, ApJ, 392, 145.
Torrelles, J.M., Ho, P.T.P, Moran, J.M., Rodríguez, L.F., Cantó J., 1986, ApJ, 307, 787.
Vrba, F. J., Luginbuhl, C. B., Strom, S. E., Strom, K. M., & Heyer, M. H. 1986, AJ, 92, 633.
Zhang, M., Brandner, W., Wang, H., Gennaro, M., Bik, A., Henning, Th., Gredel, R., Sith, M. & Stanke, Th. 2013, A&A, 553, A41.